

Electron acceleration in the dynamic magnetotail: Test particle orbits in three-dimensional magnetohydrodynamic simulation fields

J. Birn, M. F. Thomsen, and M. Hesse

Citation: [Physics of Plasmas \(1994-present\)](#) **11**, 1825 (2004); doi: 10.1063/1.1704641

View online: <http://dx.doi.org/10.1063/1.1704641>

View Table of Contents: <http://scitation.aip.org/content/aip/journal/pop/11/5?ver=pdfcov>

Published by the [AIP Publishing](#)

Articles you may be interested in

Erratum: "Defining and identifying three-dimensional magnetic reconnection in resistive magnetohydrodynamic simulations of Earth's magnetosphere" [*Phys. Plasmas* **15**, 056504 (2008)]

Phys. Plasmas **15**, 129902 (2008); 10.1063/1.2974803

Defining and identifying three-dimensional magnetic reconnection in resistive magnetohydrodynamic simulations of Earth's magnetosphere

Phys. Plasmas **15**, 056504 (2008); 10.1063/1.2913548

Three-dimensional magnetohydrodynamic simulations on the interaction of interplanetary density pulses with the bow shock


Phys. Plasmas **9**, 1764 (2002); 10.1063/1.1461847

Effect of nonzero dawn–dusk magnetic field component on particle acceleration in three-dimensional geomagnetic reconnection

Phys. Plasmas **8**, 4163 (2001); 10.1063/1.1387474


Particle acceleration in three-dimensional reconnection regions: A new test particle approach

Phys. Plasmas **6**, 4318 (1999); 10.1063/1.873696

A collection of five pieces of industrial vacuum equipment from Pfeiffer Vacuum. It includes a red rectangular turbopump, a cylindrical silver and red backing pump, a white rectangular leak detector, a red and silver measurement and analysis probe, and a silver rectangular chamber or component.

 Vacuum Solutions from a Single Source

- Turbopumps
- Backing pumps
- Leak detectors
- Measurement and analysis equipment
- Chambers and components

PFEIFFER  **VACUUM**

Electron acceleration in the dynamic magnetotail: Test particle orbits in three-dimensional magnetohydrodynamic simulation fields

J. Birn and M. F. Thomsen^{a)}

Los Alamos National Laboratory, Los Alamos, New Mexico

M. Hesse

NASA/Goddard Space Flight Center, Greenbelt, Maryland

(Received 23 October 2003; accepted 12 February 2004; published online 13 April 2004)

Electron acceleration and energetic electron flux increases in the inner tail are investigated on the basis of test-particle orbits in the dynamic fields of a three-dimensional magnetohydrodynamic simulation of neutral line formation and dipolarization in the magnetotail. Past models have mostly considered equatorial orbits, using the gyrocenter drift approximation. In this paper, the investigation is extended to include nonequatorial drifts and full orbit integrations in regions where the drift approximation breaks down. Typical acceleration mechanisms consist of betatron acceleration at large pitch angles and Fermi acceleration at small pitch angles, resulting from the dipolarization and shortening of field lines moving earthward from the neutral line. In comparison, acceleration at the near-Earth neutral line plays a negligible role in flux increases observed in the near tail. Energetic electron fluxes appear preferentially enhanced around 90° pitch angle, so that restriction to those pitch angles might lead to an overestimate of flux increases. Otherwise, the results explain the observed limitation of the range of flux enhancements between a few keV and a few hundred keV. © 2004 American Institute of Physics. [DOI: 10.1063/1.1704641]

I. INTRODUCTION

The acceleration of charged particles to high energies is an important part of activity in magnetospheric, solar, and astrophysical plasmas. Energetic particle injections into the near-Earth magnetosphere, that is, the sudden increase of charged particle fluxes at energies from tens to hundreds of keV, are a characteristic feature of the onset of the expansive phase of magnetospheric substorms [e.g., Refs. 1–3]. The particle injections are associated with a rapid reorganization of the inner magnetotail, described as dipolarization or collapse of a stretched tail-like field [e.g., Refs. 1, 4, 5] and a strong induced electric field predominantly in the dawn-to-dusk (y) direction [e.g., Ref. 6], which is localized in space as well as time. The acceleration affects both ions and electrons, but the observed signatures show local time dependence resulting from particle drifts [e.g., Ref. 7]. Surveys of dispersionless injections^{8,9} demonstrated that even the regions of dispersionless injections are not identical for electrons and ions, but most likely displaced in the east–west direction.

While modeling of the effects of wave–particle interactions requires the use of kinetic models, the acceleration from large-scale electric fields can be investigated through test particle simulations in appropriate fields [e.g., Refs. 10–15]. The observed energetic ion behavior was indeed successfully reproduced in simulations that were based on test particle orbits in the dynamic fields from an magnetohydrodynamic (MHD) simulation of tail reconnection, plasmoid ejection, and collapse of the inner tail.¹⁶ Similarly, electron

acceleration and flux changes were also investigated by test particle orbits in the same dynamic MHD simulation fields.¹⁷ These simulations, although restricted to adiabatic orbits in the equatorial plane, using the gyrocenter drift approximation, also reproduced characteristic observed energetic electron signatures and specifically, showed the east–west displacement of energetic ion and electron flux signatures and the limited energy range of flux increases. Observed temporal flux variations of energetic electrons have also been reproduced by Ref. 15, using numerical integration, and Ref. 18, using an analytic model, based on particle orbits in assumed fields modeling dipolarization of the inner tail. The two models, however, differed in the source regions for the accelerated particles.

The crucial role in generating energetic particle characteristics is played by the cross-tail electric field, induced by the dynamic changes of the tail magnetic geometry. The most important factors are that the electric field is localized in all three space dimensions, propagates earthward, and peaks near the tail/dipole transition region, rather than near the x line where reconnection takes place. In MHD simulations this property follows self-consistently from the evolution of the tail after the initiation of reconnection. Although the role of the large-scale electric field in the acceleration seems well established, it is not clear whether the properties of the particle velocity distributions, such as changes in isotropy, are the effects of the large-scale fields or whether additional smaller-scale fluctuations are crucial. As demonstrated by observations at geosynchronous orbit, preexisting perpendicular anisotropies ($T_\perp > T_\parallel$) of thermal ions and electrons typically decrease during the substorm growth phase and increase again after onset,⁸ while energetic electron distribu-

^{a)}Electronic mail: jbirn@lanl.gov

tions become more field aligned during the growth phase and less field aligned after onset. The study of such effects obviously requires consideration of arbitrary pitch angles and nonequatorial orbits. This is also necessary in order to estimate pitch-angle-integrated fluxes, which may differ from strictly equatorial fluxes.

Most of the earlier investigations of electron injections have been based on adiabatic drift orbits, using the conservation of the magnetic moment [e.g., Refs. 15, 18]. This approximation is usually well satisfied for electrons in the vicinity of geosynchronous orbit, where most of the injection observations have been made. However, encounters of the neutral sheet under sufficiently weak fields do not satisfy the drift approximation. Such encounters act like a pitch-angle scattering process [e.g., Ref. 19], such that orbits that are initially close to the equatorial plane need not stay close to that plane, or vice versa. Furthermore, substorm simulations indicate that the collapse of the inner tail is the consequence of magnetic reconnection farther downtail [e.g., Ref. 20], presumably at a distance around 20 to 30 R_E . Reconnection shortens magnetic field lines, reduces the specific entropy, and thus enables the transport into the inner tail [e.g., Ref. 21–23]. Collapsing field lines, identified by reduced entropy content, hence typically have previously undergone reconnection. Energetic electrons up to energies of tens or hundreds of keV typically also follow this field line history. That means that prior to the collapse, these electrons typically have passed the vicinity of the reconnection site, where the drift assumption breaks down. This becomes important when the effects of the collapse are to be compared with the direct acceleration in the vicinity of the neutral line, for the identification of the source regions, and for a quantitative estimation of fluxes when the injected particles have to be traced back to the source configuration prior to the initiation of the dynamic phase. Therefore, a full investigation of the history of accelerated electrons in the dynamic reconnecting tail has to take into account that during parts of that history the adiabatic drift assumption may not be valid, so that full orbit integrations have to be made.

As in our previous test particle investigations,^{16,17} we use the electric and magnetic fields obtained from an MHD simulation.²⁰ This simulation includes both features considered as potentially relevant for particle acceleration: a neutral line region associated with the reconnection process and the field collapse or dipolarization of the inner tail (which is similar to the “convection surge mechanism”^{24,25}). This has already permitted a comparison of the relative importance of these features for ion acceleration. While both mechanisms were found to contribute to ion acceleration and enhancement of fluxes, the electric field associated with the collapse was most significant for the initial flux increase of an injection and hence the inner (earthward) edge of the region of enhanced ion fluxes (injection boundary). Here, we extend this work to consider electron acceleration.

In Sec. II we will discuss the equations of motion. Full orbit integration of the electron motion is time consuming and unnecessary in regions where electrons are adiabatic, and may actually lead to unwanted large accumulated errors. We therefore switch from full orbits to drift orbits, and vice

versa, when the drift approximation becomes valid or invalid. In Sec. III we will describe characteristics of the simulation fields and illustrate typical orbits and acceleration mechanisms. Section IV then will be devoted to phase-space variations of the simulated electron fluxes.

II. BASIC APPROACH

The electron energies of interest approach or may even exceed the rest energy. We therefore use relativistic equations of motion. The full motion of an electron with rest mass m_e and charge $-e$ is described by

$$\frac{D\mathbf{u}}{Dt} = -\frac{e}{m_e} \left(\mathbf{E} + \frac{1}{\gamma} \mathbf{u} \times \mathbf{B} \right), \quad (1)$$

where

$$\frac{D}{Dt} \equiv \frac{\partial}{\partial t} + \mathbf{w} \cdot \nabla. \quad (2)$$

Here, we have set $\mathbf{u} = \gamma \mathbf{w}$, where \mathbf{w} is the electron velocity, and

$$\gamma = \frac{1}{\sqrt{1 - w^2/c^2}} = \sqrt{1 + u^2/c^2}, \quad (3)$$

is the relativistic factor. The kinetic energy of the electron is then given by

$$W_{\text{kin}} = (\gamma - 1)m_e c^2. \quad (4)$$

The drift of an electron with rest mass m_e (relativistic) magnetic moment μ_r , and charge $q = -e$ is given by [e.g., Ref. 26]

$$\begin{aligned} \mathbf{v}_d = \mathbf{v}_E - \frac{\mu_r}{\gamma e} \frac{\mathbf{B} \times \nabla B}{B^2} - \frac{m_e \gamma v_{\parallel}}{e} \frac{\mathbf{B}}{B^2} \times \frac{d\mathbf{b}}{dt} - \frac{m_e}{e} \frac{\mathbf{B}}{B^2} \\ \times \frac{d\gamma \mathbf{v}_E}{dt}, \end{aligned} \quad (5)$$

where $\mathbf{b} \equiv \mathbf{B}/B$

$$\mathbf{v}_E = \frac{\mathbf{E} \times \mathbf{B}}{B^2}, \quad (6)$$

and

$$\frac{d}{dt} \equiv \frac{\partial}{\partial t} + (\mathbf{v}_{\parallel} + \mathbf{v}_d) \cdot \nabla, \quad (7)$$

is the time derivative along the drift orbit. The relativistic magnetic moment μ_r is defined by

$$\mu_r = \frac{p_{\perp}^2}{2m_e B}, \quad (8)$$

where $p_{\perp} = m_e \gamma w_{\perp} = m_e u_{\perp}$ is the perpendicular relativistic momentum associated with the gyration speed w_{\perp} . The kinetic energy is then given by (4) with

$$\gamma = \sqrt{1 + (u_{\parallel}^2 + 2\mu_r B/m_e + u_E^2)/c^2}, \quad (9)$$

where $u_{\parallel} = \gamma v_{\parallel}$ and $\mathbf{u}_E = \gamma \mathbf{v}_E$. We note that we do not distinguish between the parallel speed of the particle and that of

the gyrocenter. The drift contributions are neglected in the energy expression (9) because these contributions are even smaller than the $\mathbf{E} \times \mathbf{B}$ drift contribution in comparison to those of the gyromotion and the parallel motion.

Concerning the equation of motion for the parallel component of the velocity, it turns out that the expression given, for instance, in Ref. 26 has to be modified to ensure exact energy conservation for stationary fields. The additional terms are only of order ϵ^2 , where ϵ is the smallness parameter of the adiabatic expansion (say, the ratio of a gyroperiod over a macroscopic time scale). Nevertheless, this correction becomes relevant when drift orbits are followed over times corresponding to many gyrations. The corrected equation of motion can be derived from a Hamiltonian approach.²⁷ It is given by

$$\frac{du_{\parallel}}{dt} = -\frac{e}{m_e} E_{\parallel} - \frac{\mu_r}{\gamma m_e} \frac{\partial B}{\partial s} + (\mathbf{u}_E + \mathbf{u}_{\nabla B}) \cdot \frac{d\mathbf{b}}{dt}. \quad (10)$$

Here, $\mathbf{u}_{\nabla B} = \gamma \mathbf{v}_{\nabla B}$, and $\mathbf{v}_{\nabla B}$ is the gradient B drift given by the second term on the right-hand side of (5).

To estimate the relative order of magnitude of the terms in (5) and (10), we normalize them using characteristic quantities B_c , t_c , and v_c as defined in the MHD run. Here, $B_c = 80$ nT is the lobe field strength at the inner boundary of the simulation box, $t_c = 6$ s is a characteristic Alfvén wave travel time across the plasma sheet with a half thickness of $L_c = 1 R_E$ at the inner boundary, and $v_c = L_c/t_c \approx 1000$ km/s is a typical Alfvén speed. The corresponding electric field unit is $E_c = B_c v_c$. We normalize the magnetic moment of the electron using the same energy unit as in our previous study¹⁷ and in the study of proton orbits,¹⁶ because we are interested in similar energies

$$W_c = \frac{m_p}{2} v_c^2 \approx 5 \text{ keV}, \quad (11)$$

such that $\mu_c = W_c/B_c$. Typical dimensionless values of the energies and magnetic moments of energetic particles are in the range 10–100 (corresponding to 50–500 keV).

Equation (5) then can be written in dimensionless form (using the symbol $\hat{\cdot}$ to denote dimensionless quantities)

$$\hat{\mathbf{v}}_d = \hat{\mathbf{v}}_E - \frac{\epsilon \hat{\mu}}{2\gamma} \frac{\hat{\mathbf{B}} \times \nabla \hat{B}}{\hat{B}^2} - \epsilon \sigma \hat{u}_{\parallel} \frac{\hat{\mathbf{B}}}{\hat{B}^2} \times \frac{d\mathbf{b}}{d\hat{t}} - \epsilon \sigma^2 \frac{\hat{\mathbf{B}}}{\hat{B}^2} \times \frac{d\hat{\mathbf{u}}_E}{d\hat{t}}, \quad (12)$$

where $\hat{u}_{\parallel} = u_{\parallel}/v_c$

$$v_{ce} = v_c \sqrt{m_p/m_e}, \quad (13)$$

$\sigma = \sqrt{m_e/m_p} = 1/42.85$, and ϵ represents the ratio between the proton gyroperiod (divided by 2π) and the characteristic Alfvén time t_c , given by

$$\epsilon = 1/(\omega_c t_c) = m_p/(e B_c t_c). \quad (14)$$

For typical tail parameters, $\epsilon \approx 1/50$.

The last term in (12), representing electron inertia effects, is typically much smaller than the preceding gradient drift term, as indicated by the additional factor σ . This term is therefore neglected. The electron drift equations used here hence are given by

$$\hat{\mathbf{v}}_d = \hat{\mathbf{v}}_E - \frac{\epsilon \hat{\mu}}{2\gamma} \frac{\hat{\mathbf{B}} \times \nabla \hat{B}}{\hat{B}^2} - \epsilon \sigma \hat{u}_{\parallel}^2 \frac{\hat{\mathbf{B}}}{\hat{B}^2} \times \frac{\partial \mathbf{b}}{\partial \hat{s}}, \quad (15)$$

$$\frac{d\hat{u}_{\parallel}}{d\hat{t}} = -\frac{1}{\epsilon \sigma} \hat{E}_{\parallel} - \frac{\hat{\mu}}{2\sigma \gamma} \frac{\partial \hat{B}}{\partial \hat{s}} + \frac{\hat{u}_{\parallel}}{\gamma} (\hat{\mathbf{u}}_E + \hat{\mathbf{u}}_{\nabla B}) \cdot \frac{\partial \mathbf{b}}{\partial \hat{s}}, \quad (16)$$

where $\hat{\mathbf{v}}_{\nabla B} = \mathbf{v}_{\nabla B}/v_c$ and only the leading term of $d\mathbf{b}/dt$ is retained.

The (normalized) kinetic energy of an electron in the drift approximation is given by

$$\hat{W} = 2(\gamma - 1)c^2/v_{ce}^2, \quad (17)$$

where

$$\gamma = \sqrt{1 + (v_{ce}^2/c^2)(\hat{u}_{\parallel}^2 + \hat{\mu} \hat{B} + \sigma^2 \hat{u}_E^2)}. \quad (18)$$

The factor σ^2 in the last term in (18) stems from the fact that the parallel velocity, as well as the gyration speed are normalized by v_{ce} , while the $\mathbf{E} \times \mathbf{B}$ drift velocity is normalized by v_c . Clearly, the first terms in (18) dominate for kinetic energies larger than approximately 1 keV, as considered here. The $\mathbf{E} \times \mathbf{B}$ drift term will therefore also be neglected in (18). This neglect is consistent with the neglect of the inertia term in (15).

The drift approximation breaks down when the gyroperiod becomes comparable to the characteristic time for the field evolution, t_c , or when the gyroradius becomes comparable to the characteristic length scale of the underlying electric and magnetic field. The first condition leads to a limit for the magnetic field strength, which can be written in dimensionless form as

$$\hat{B}_{cr1} = \lambda_1 \epsilon \sigma^2 \approx \lambda_1 10^{-5}, \quad (19)$$

where λ_1 is a numerical factor large compared to unity, say, $\lambda_1 \approx 100$. The drift approximation thus breaks down when the magnetic field strength becomes smaller than $\hat{B}_{cr1} \approx 10^{-3}$.

In the evaluation of the second condition, we find that typically the shortest characteristic length scale near the equatorial plane is the magnetic field curvature radius r_c . A conservative estimate therefore is that the drift approximation is valid when

$$a < r_c/\lambda_2, \quad (20)$$

where a is the local gyroradius and λ_2 is a number of order 10 or larger. At the equatorial plane, the curvature radius is approximately given by $r_c = (B_z/B_c)L_c$, where B_c and L_c are the characteristic lobe field and plasma sheet half-thickness defined earlier, respectively, and the gyroradius by $a = m_e v_{\perp}/(e B_z)$, where v_{\perp} is the gyration velocity. In dimensionless form, this leads to a second condition for the magnetic field, given by

$$\hat{B}^2 > \hat{B}_{cr2}^2 = \lambda_2 \epsilon \sigma u_{\perp} = \hat{u}_{\perp}/u_{cr}, \quad (21)$$

where $u_{\perp} = \gamma v_{\perp}$ and we have replaced B_z with B to apply this criterion to arbitrary locations. After some numerical experiments we chose $u_{cr} = 1/(\lambda_2 \epsilon \sigma) = 100$.

The condition (21) is usually much more stringent than that given by threshold (19), except at very low energies. The

threshold value B_{cr} for transition to a full orbit is also higher than the one used by Ref. 17, due to the fact that the orbits in that paper were confined to 90° pitch angle in the equatorial plane such that the curvature drift vanishes. The gradient B drift is typically much smaller in the stretched tail, extending the limit for the validity of the drift approximation to lower B values.

For $B < B_{cr}$ the full orbits are integrated. Using the same normalization as before, the full equations of motion are given by

$$\frac{D\hat{\mathbf{r}}}{D\hat{t}} = \frac{1}{\sigma} \hat{\mathbf{u}}, \quad (22)$$

$$\frac{D\hat{\mathbf{u}}}{D\hat{t}} = \frac{1}{\epsilon\sigma^2} (\sigma\hat{\mathbf{E}} + \gamma\hat{\mathbf{u}} \times \hat{\mathbf{B}}), \quad (23)$$

where $\hat{\mathbf{u}} = \gamma\mathbf{w}/v_{ce}$. Note that the vectors \mathbf{r} and \mathbf{w} now denote the particle location and velocity, respectively, and that \mathbf{E} and \mathbf{B} are evaluated at this location. Also, D/Dt denotes the derivative along the full orbit, given by (2), rather than along the drift orbit. The condition $\hat{B} < \hat{B}_{cr}$, where B_{cr} is the maximum of the values given by (19) and (21), is used to switch from drift orbit integration to full orbit integration. To avoid a too-frequent shifting when \hat{B} oscillates around the critical value, we increased the critical value for upward shifting (from full orbit to drift) by a factor of 1.5.

When switching from a full orbit to the drift approximation, the phase information is lost. At the switch from drift to full orbit we therefore imposed a random phase. Although the choice of this phase may strongly affect an individual orbit, we found that it had no significant effect on the overall characteristics, such as the times and locations where accelerated particles are found. Similarly, the exact numerical value for the critical magnetic field strength \hat{B}_{cr} for the orbit shift, which also influences the phase, may significantly alter an individual orbit but has no strong effect on the overall characteristics. This will be discussed in the following section.

III. BACKGROUND FIELDS AND CHARACTERISTIC ORBITS

The underlying MHD simulation²⁰ is the same as in previous test particle investigations,^{16,17} modeling the dynamics of a tail section $-65 R_E \leq x \leq -5 R_E$, $|y| \leq 10 R_E$, $|z| \leq 10 R_E$, with a dipole located outside the simulation box at $x=0$ and assuming symmetry around $y=0$ and $z=0$. The simulation of the dynamic breakup phase is preceded by a simulated growth phase, during which an external electric field is applied at the high-latitude boundary of the simulation box. This leads to the formation of a thin current sheet in the near tail, characteristic for the late growth phase and presumably crucial for the initiation of the breakup phase. The breakup of this current sheet is initiated by imposing finite resistivity, defining the initial time $t=0$. A magnetic neutral line forms ~ 2 min after imposing the resistivity. Important features are illustrated in Fig. 1, which shows the color-coded magnetic field B_z in the equatorial plane for $t=6-9$ min. The red contour represents the neutral line B_z

$=0$, and black lines are contours of constant positive E_y , spaced at intervals of 4 mV/m. Figure 1 shows the strong localization of the dipolarization and of the enhanced E_y with a peak located well earthward of the neutral line. This is the region that most strongly affects the orbits and the particle acceleration.

Since the MHD results are given on a finite grid that is coarser than the orbit integration steps, interpolation of the MHD fields in space and time is necessary. The electric and magnetic fields were interpolated linearly in time. Consistency between the magnetic field gradients in (15) and (16) and the interpolated fields and continuity at the boundaries of the grid boxes requires that the magnetic field be interpolated by third-order polynomials in the space coordinates. Since this can introduce spurious nonmonotonic variations of the interpolated variables when the fields vary rapidly in space, a monotonicity-preserving algorithm was used to constrain the derivatives of \mathbf{B} .²⁸ The electric field was interpolated linearly in space.

As in our previous test particle simulations, we integrated the particle orbits backwards in time until they reached the boundary of the simulation box or the initial state. This enables us to impose initial and boundary distributions, consistent with the MHD moments, and to infer the distribution function at the later time via Liouville's theorem of the conservation of the phase-space density f along the particle trajectory. While this procedure works very well when the phase-space mapping between the initial and final locations is a smooth function of the phase coordinates,²⁹ chaotic effects may dominate in parts or all of phase space. That means that a slight variation in the final location or speed can lead to vastly different initial locations or speeds, and vice versa. Similar effects may arise from the choice of the random phase at transitions from a drift orbit to a full orbit. In this case the mapped value of the distribution function can fluctuate significantly in a small neighborhood of the chosen phase-space location. The actual value to be compared with observations then has to be an average of f over such a neighborhood, using a sufficient number of phase-space trajectories.

A. Effect of the threshold for orbit transitions

Typical effects of orbit transitions and the role of the critical threshold (21) are illustrated by Fig. 2, which shows the equatorial crossing points of orbits traced backwards in time from $t=8$ min at $x=-10$, $y=z=0$ with a final pitch angle of 85° and an energy of 180 keV. Since the final part of the orbit satisfied our drift criterion, no phase specification was necessary. The orbits are superposed on contours of constant cross-tail electric field, as shown in Fig. 1, taken at $t=7$ min. Orbit (a) (red curve) corresponds to the choice $u_{cr}=100$ in (21), while orbits (b) and (c) (green and blue curves, respectively) correspond to $u_{cr}=200$, but with slightly different pitch angles. The dots mark the transition from full orbits to drift orbits, or vice versa in each case. All curves show qualitatively similar histories, consisting (forward in time) of a drift from the boundary $y=10$ towards the center, a somewhat erratic portion near $y=2$, where the particles encounter the strong spatial and temporal gradients of

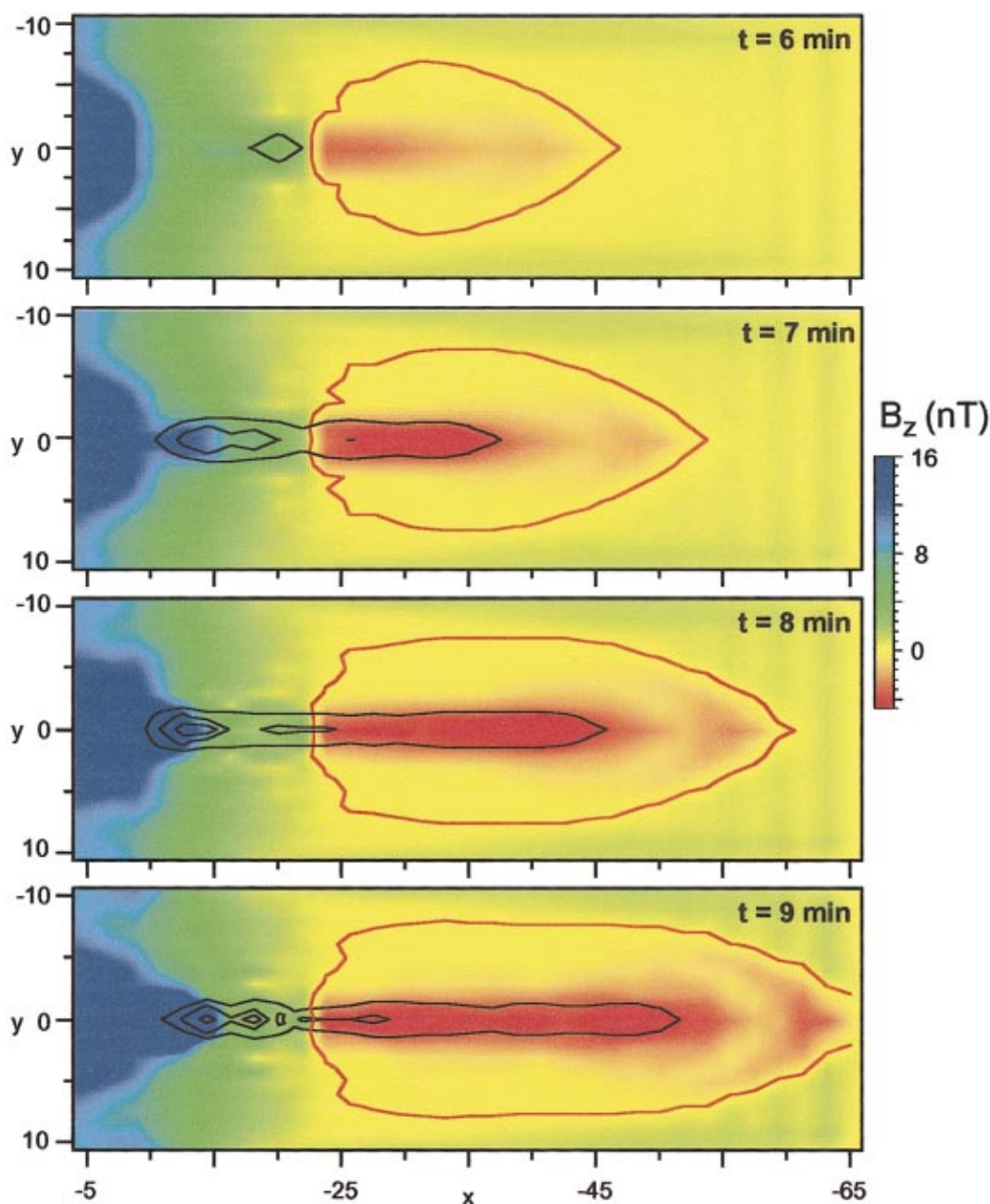


FIG. 1. (Color) Color-coded magnetic field B_z in the equatorial plane for $t=6-9$ min, as obtained in the underlying MHD simulation (Ref. 20). The red contour represents the neutral line $B_z=0$, and black lines are contours of constant positive E_y , shown at multiples of 4 mV/m.

the electric and magnetic field, and a final earthward drift towards the chosen end location. The late history ($-10 \geq x \geq -13$) of orbits (a), (b), and (c) is very similar, despite the fact that most of this section is calculated using the drift approximation for orbits (b) and (c), while full orbits are calculated during the neutral sheet crossings for orbit (a). The orbits begin (backwards in time) to deviate from each other near the location $x = -13.5$, $y = 2$. This is an effect of a sensitivity to small differences in the phase-space locations, rather than a sensitivity to the value of u_{cr} . To demonstrate this, we included orbit (c) in Fig. 2 (blue curve), which corresponds to the same value $u_{cr}=200$ as orbit (b) but a slightly different final pitch angle ($\alpha=85.0001^\circ$). This orbit begins to deviate from the others near the same location,

eventually following an early history ($y > 2$) closer to orbit (a) than orbit (b). The energy gain for cases (a)–(c) was 124.8, 125.7, and 140.9 keV, respectively. In this case, the change in the value of u_{cr} has (accidentally) less effect on the energy gain than the change in the final pitch angle.

In summary, the effects of changing the threshold value B_{cr} are comparable to the effects of small changes in the phase-space coordinates. Orbits that are sensitive to such changes are also sensitive to the changes of B_{cr} , while orbits that are insensitive to small variations of the initial or final phase-space location are also insensitive to a variation of B_{cr} . However, although such variations thus may have a significant effect on some individual orbits, we found no

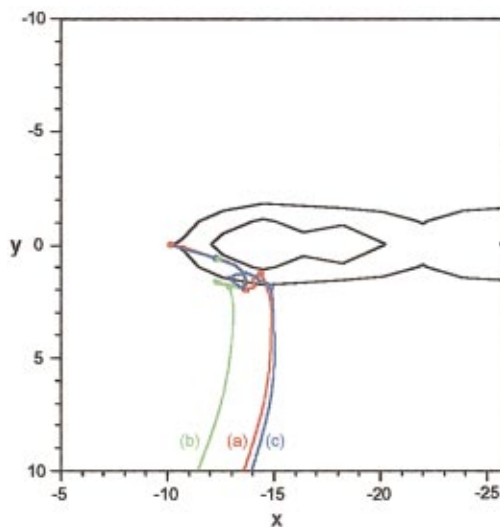


FIG. 2. (Color) Equatorial crossing points of orbits traced backwards in time from $t=8$ min at $x=-10$, $y=z=0$ with a final pitch angle of $\alpha=85^\circ$ and an energy of 180 keV. The orbits are superposed on contours of constant cross-tail electric field (black lines), taken at $t=7$ min. Orbit (a) (red curve) corresponds to $u_{cr}=100$ in (21), while orbits (b) and (c) (green and blue curves, respectively) correspond to $u_{cr}=200$, and pitch angles $\alpha=85^\circ$ and $\alpha=85.0001^\circ$. The dots mark the transition from full orbits to drift orbits, or vice versa in each case.

strong effect on the general characteristics of fluxes to be discussed later.

B. Characteristic acceleration

Figure 3 illustrates the typical acceleration of electrons. The top part of each figure shows sections of a characteristic electron orbit in a perspective view from the earthward side, whereas the bottom parts show the magnitude of the particle energy above the equatorial crossing points of the orbit. Figure 3(a) illustrates the most typical orbit of accelerated elec-

trons with energies above approximately 100 keV. The electron originates from the duskward boundary, bounces many times between the mirror points (or between the reflection points at the boundary $x=-5$ when the pitch angle is smaller), while drifting towards the center tail. When it reaches the central region of earthward collapse it participates in the drift and becomes accelerated through a betatron or Fermi mechanism, depending on the pitch angle. Except for the bounce motion, this is similar to the history of typical 90° pitch-angle accelerated electrons investigated in Ref. 17.

A variant of this history is shown by Fig. 3(b) for a different final pitch angle. This particle also starts from the dusk boundary but from an orbit with an equatorial crossing point farther out, tailward of the reconnection site. When this particle approaches the center tail, it becomes trapped on the earthward section of a field line that undergoes reconnection. Subsequently, it participates also in the earthward collapse. The bottom part of Fig. 4 shows that essentially all of the acceleration takes place during this collapse.

Figure 3(c) shows an orbit that is more typical at lower energies of tens of keV. Since the cross-tail drift is less significant at these energies, the electrons typically start out inside the boundaries at the initial tracking time. The particle drifts slowly earthward and toward the center until it reaches the inner tail region and participates in the earthward drift. Again, this is the part of the major acceleration.

All orbits shown in Fig. 3 share the fact that the major acceleration occurs while the electron participates in the earthward convection of dipolarizing field lines. When the pitch angle is close to 90° this can easily be understood as betatron acceleration. When the pitch angle is smaller, the acceleration can also be understood as an adiabatic process, namely Fermi acceleration of a particle that bounces between mirror points within a flux tube that becomes shorter as it dipolarizes and moves towards the Earth. This is a combination of Fermi type "A" and type "B",²⁶ where type A cor-

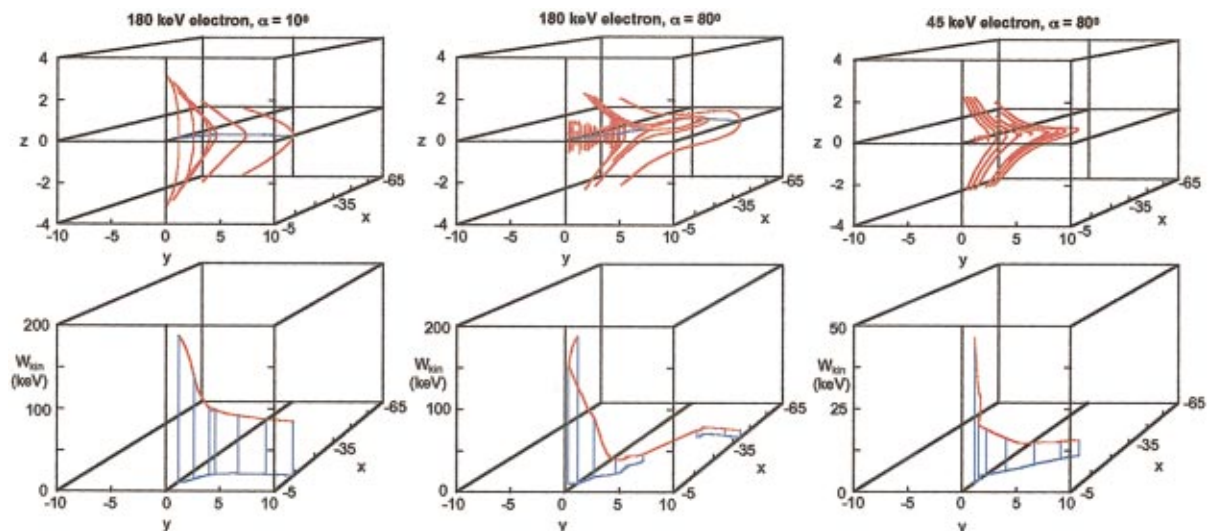


FIG. 3. (Color) Characteristic orbits traced backwards in time from $x=-10 R_E$, $y=0$, $z=0$. The top parts show selected bounce orbits in a perspective view from the earthward side (red lines) above the equatorial crossing points of the orbit (blue line), whereas the bottom part shows the magnitude of the particle energy (red line) above the equatorial crossing points (blue line). The figures correspond to (a) a final energy of 180 keV and a pitch angle $\alpha=15^\circ$; (b) 180 keV and $\alpha=80^\circ$; and (c) 180 keV and a $\alpha=15^\circ$, respectively.

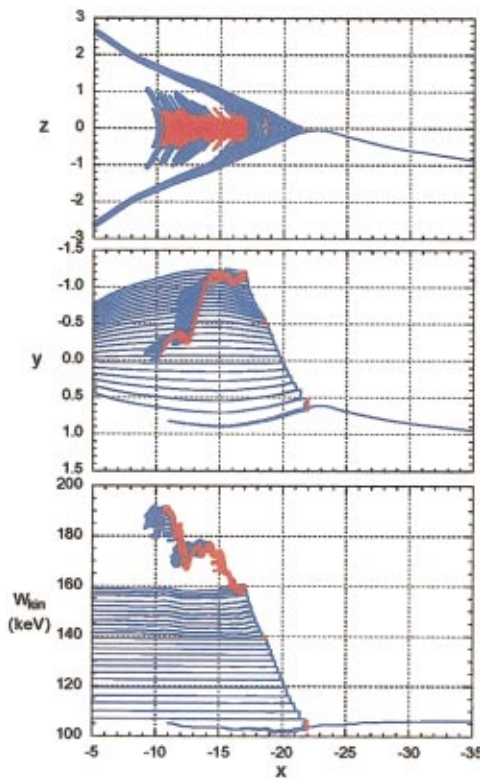


FIG. 4. (Color) Electron orbit integrated backwards from $t=7$ min at $x=-10$, $y=0$, $z=0$ with a final energy of 180 keV and pitch angle of 45° . The top panels show different projections of the orbit, and the bottom panel shows the energy above the location in x . Red portions of the orbit belong to full orbit integration.

responds to the effects of particle reflection in a mirror field, while type B denotes the effects of field-aligned motion along a moving curved magnetic field line, such as those crossing the neutral sheet. This is illustrated by the orbit shown in Fig. 4, which is integrated backwards from $t=7$ min at $x=-10$, $y=0$, $z=0$ with a final energy of 180 keV and pitch angle of 45° . The top panels show different projections of the orbit, and the bottom panel shows the energy above the location in x . Red portions of the orbit belong to full orbit integration. It is obvious from this figure that, in the fixed frame, the acceleration takes place exclusively during the neutral sheet traversals, because that is the region where the electric field is concentrated. It does not matter whether the full orbit is integrated or the drift approximation is used. This shows that the acceleration at small pitch angles resembles Fermi type-B acceleration, which is equivalent to neutral sheet or current sheet acceleration, as discussed by Ref. 30. In this frame, the mirroring closer to the Earth does not change the energy but is important in providing multiple neutral sheet crossings. However, in a frame that moves with the equatorial crossing point of the field line, the particle acceleration results from the reflection at the moving mirrors, so that the whole process is indeed a combination of type-A and type-B Fermi acceleration.

IV. CHARACTERISTICS OF PHASE-SPACE DISTRIBUTIONS

In this section we will investigate characteristic pitch-angle variations at various energies. In order to compare flux

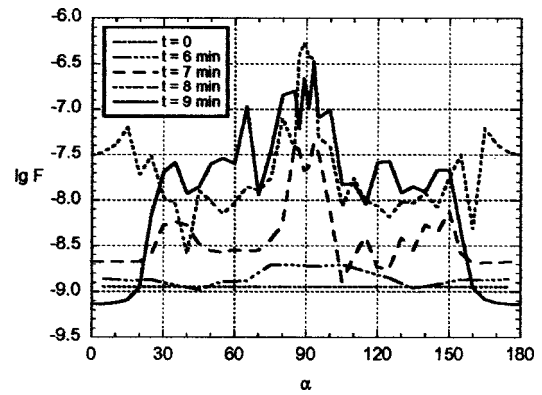


FIG. 5. Pitch-angle variation of the phase-space distribution f at $x=-10$, $y=0$, $z=0$ for an energy of 180 keV and various times as indicated.

levels at different energies, we need to evaluate the values of the distribution function f . This can be done by using Liouville's theorem of the conservation of f along the phase-space trajectory and imposing initial and boundary distributions consistent with the moments of the MHD simulation. We use the same initial and boundary distributions as in our previous investigation of equatorial electron orbits,¹⁷ defined as kappa distributions^{31,32}

$$f = \hat{f} \left[1 + \frac{E}{(\kappa - 1.5)E_o} \right]^{-\kappa - 1}, \quad (24)$$

with

$$\kappa = 2.5, \quad E_o = 0.5 \text{ keV}, \quad (25)$$

neglecting again spatial variations of the characteristic parameters in (24). Since the plasma sheet density and temperature in the MHD run do not vary strongly, this neglect has little effect when particles originate from the plasma sheet. Also, the earthward beams of particles in the plasma sheet boundary layer have similar value of the phase-space density. However, the plasma in the lobes is significantly cooler and more tenuous than the plasma sheet plasma, so that the mapped flux values should be reduced when particles originate from the lobes. This becomes important primarily for electrons at energies below ~ 100 keV at later times, when lobe field lines reconnect.

Figure 5 shows the pitch-angle variation of the phase-space distribution f at the location $x=-10$, $y=0$, $z=0$ for an energy of 180 keV and various times as indicated. There are strong pitch-angle anisotropies, which may vary as a function of time, but with a preference for enhanced fluxes near 90° pitch angles. This region widens with time. Figure 6 demonstrates that this feature persists over a wide energy range, by showing the pitch-angle variation of f at $t=8$ min at the same location for energies between 5 and 500 keV. At lower energies, additional peaks near 0° and 180° become evident, which are even higher than the peak near 90° .

In principle, the distributions in Figs. 5 and 6 should be exactly symmetric around $\alpha=90^\circ$, if the starting phase locations were exactly symmetric. However, due to the random phase shifts at orbit transitions, and to the aforementioned chaotic effects, individual orbits can vary significantly from

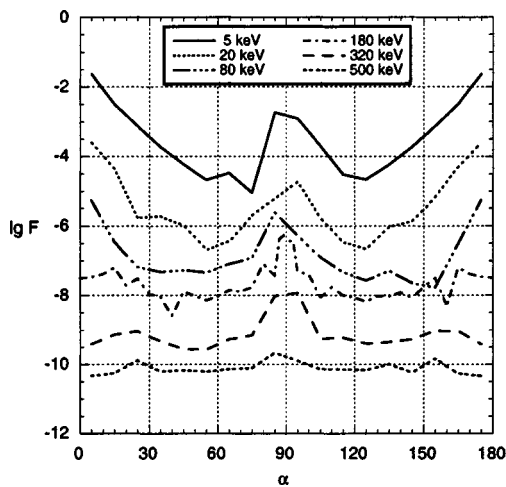


FIG. 6. Pitch-angle variation of the phase-space distribution f for $t=8$ min at $x=-10$, $y=0$, $z=0$, and energies between 5 and 500 keV, as indicated.

their symmetry partners. Nevertheless, the main features of the figures are quite symmetric and consistent on either side of $\alpha=90^\circ$. A similar result was obtained when we changed the value of the transition parameter u_{cr} in (21).

The preferential enhancement of fluxes around 90° pitch angles suggests that an investigation of those pitch angles alone might result in an overestimation of flux increases. This is confirmed by Fig. 7, which shows electron distribution functions, averaged over 18 pitch angles, at $x=-10$, $y=0$, $z=0$ before ($t=6$ min) and after the injection ($t=7$ min), calculated from an initial kappa distribution (dotted line). For comparison, we also include the distribution of 90° electrons, as obtained in Ref. 17. This clearly demonstrates that consideration of 90° pitch-angle electrons alone may lead to a considerable overestimate of fluxes, whereas the main temporal features, particularly the rise of fluxes, may be similar. The change in the model distribution function in Fig. 7 is quite similar to the changes in observed distributions shown in Ref. 17. Flux increases occur only in a limited energy range, which extends from about 1 to 500 keV in the simulation.

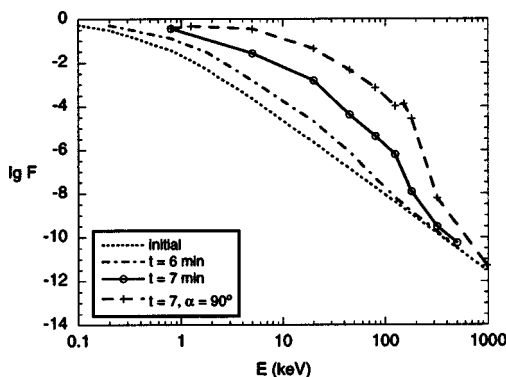


FIG. 7. Electron distribution function at $x=-10$, $y=0$, $z=0$ before ($t=6$ min; dash-dotted line) and after the injection ($t=7$ min; solid line), calculated from an initial kappa distribution (dotted line), averaged over 18 pitch angles. For comparison, the distribution of 90° electrons, as obtained in Ref. 17, is also included (dashed line).

Similar to results obtained for 90° pitch angles, the distribution function in Fig. 7 at $t=6$ min is already distorted from the source distribution by an increase that ranges from a few keV to ~ 50 keV. Again, this may be attributed to an early weaker increase of the electric field, which may even occur during the substorm growth phase. This is also consistent with observations.⁸

V. SUMMARY AND CONCLUSIONS

Extending previous work,¹⁷ we have investigated properties of substorm-associated electron injections on the basis of test particle simulations in the time-dependent magnetic and electric fields of an MHD simulation of magnetotail dynamics.²⁰ This MHD simulation combines self-consistently the two main features commonly considered for particle acceleration in the inner magnetotail: a near-Earth x-type magnetic neutral line, located approximately at $18 R_E$ from the near-Earth boundary of the simulation box ($23 R_E$ from the center of the dipole), and the collapse and dipolarization of the innermost tail region earthward from the neutral line. The strongest induced electric fields develop in this region rather than in the immediate vicinity of the neutral line.

In the previous investigation¹⁷ we considered only electron orbits in the equatorial plane, which is a symmetry plane of the MHD simulation. Here, we extended the analysis to arbitrary pitch angles and off-equatorial orbits. Also, we switched between gyrocenter drift orbits and full orbit integration depending upon the validity of the drift approximation. This happens primarily at neutral sheet crossings relatively close to the near-Earth neutral line. Higher-energy electrons (hundreds of keV) that contribute to the flux increases in the near tail typically did not approach the neutral line very closely during their history, due to their strong cross-tail drift. In contrast, lower-energy electrons (a few keV to tens of keV) follow more closely the history of field line “motion,” as given by the $\mathbf{E} \times \mathbf{B}$ drift. They have hence been close to the neutral line, while the field line was undergoing reconnection. As a paradoxical consequence, full orbit integration thus becomes necessary at lower energies, during part of the orbit, while the drift approximation can be applied fully for many of the higher-energy orbits.

As in our earlier investigations,^{16,17} we found that acceleration in the inner collapsing tail region is relatively more important for flux increases in the near tail than the energy gain from the cross-tail motion near the neutral line. For particles in the vicinity of the equatorial plane with pitch angles close to 90° , this acceleration can be understood as betatron acceleration. Particles with small pitch angles can be viewed as following a collapsing field line through many bounces. Since the field line becomes shorter as it dipolarizes and approaches the Earth, the acceleration mechanism can be understood as Fermi acceleration. An investigation of the acceleration during such a multiple bounce orbit shows that the acceleration, in a fixed frame, takes place during the relatively short neutral sheet crossing, where the large cross-tail electric field is localized. The acceleration of the small pitch-angle electrons hence can be understood as multiple Fermi

type-B acceleration,²⁶ equivalent to neutral sheet or current sheet acceleration, as discussed in Ref. 30. In a frame that moves with the equatorial crossing point of an earthward convecting field line, the acceleration results from the reflection at the moving mirrors, corresponding to Fermi type-A acceleration,²⁶ so that the whole process is a combination of both types.

The dominant source region of accelerated electrons at higher energies (above ~ 100 keV) is the dusk flank plasma sheet, primarily earthward of the neutral line, although the more distant plasma sheet and plasma sheet boundary layer may also contribute. This explains why models that concentrate on equatorial drift orbits only^{15,17,18} still capture the dominant mechanism. In contrast, the more distant plasma sheet and the plasma sheet boundary layer are the more dominant source at lower energies and at the beginning of reconnection, before lobe reconnection starts (note that lobe reconnection starts later at larger $|y|$).

Although we found that electrons can become accelerated at both small and large pitch angles, through Fermi and betatron acceleration, respectively, the effects may differ. At the specific location considered, near the earthward edge of the injection region, we find an anisotropy with enhanced fluxes at both small and large (near 90°) pitch angles but reduced or unchanged fluxes at intermediate angles. The enhancement near 90° is more pronounced, so that the net result might be an enhancement of perpendicular pressure. However, pitch-angle scattering mechanisms, resulting from small-scale fluctuations not contained in the MHD model, could reduce or even eliminate the pitch-angle dependence of the flux increases.

In summary, the results obtained by generalized orbit integration confirm the results obtained earlier by equatorial drifts only. The effects of the MHD fields on the test electrons thus can explain major features of electron injections, specifically the limited energy range and the relative amount of the flux increases. This further supports the view that the mechanisms of cross-tail acceleration and field collapse or dipolarization of the inner tail ("convection surge mechanism"^{24,25}) are the major mechanisms responsible not only for ion acceleration and injection but also for electron injections in the inner magnetotail. The test orbits show that the electric field associated with the collapse is most significant for the inner edge of the region of enhanced electron fluxes (injection boundary), as well as for the ion injection boundary.¹⁶

ACKNOWLEDGMENTS

This work was supported by the U.S. Department of Energy's Office of Basic Energy Sciences through its Geosciences Research Program and by NASA's Sun Earth Connection Theory Program.

- ¹T. W. Lezniak and J. R. Winckler, *J. Geophys. Res.* **75**, 7075 (1970).
- ²D. N. Baker, P. R. Higbie, E. W. Hones, Jr., and R. D. Belian, *J. Geophys. Res.* **83**, 4863 (1978).
- ³K. N. Erickson, R. L. Swanson, R. J. Walker, and J. R. Winckler, *J. Geophys. Res.* **84**, 931 (1979).
- ⁴W. D. Cummings, J. N. Barfield, and P. J. Coleman, *J. Geophys. Res.* **73**, 6687 (1968).
- ⁵B. T. Thomas and P. Hedgecock, "Substorm effects in the neutral sheet inside $10 R_E$," in *Magnetospheres of the Earth and Jupiter*, edited by P. Formisano (Reidel, Norwell, MA, 1975), p. 55.
- ⁶T. L. Aggson, J. P. Heppner, and N. C. Maynard, *J. Geophys. Res.* **88**, 3981 (1983).
- ⁷G. D. Reeves, R. D. Belian, and T. A. Fritz, *J. Geophys. Res.* **96**, 13997 (1991).
- ⁸J. Birn, M. F. Thomsen, J. E. Borovsky, G. D. Reeves, D. J. McComas, and R. D. Belian, *J. Geophys. Res.* **102**, 15345 (1997).
- ⁹M. F. Thomsen, J. Birn, J. E. Borovsky, K. M. Morzinski, D. J. McComas, and G. D. Reeves, *J. Geophys. Res.* **106**, 8405 (2001).
- ¹⁰M. Ashour-Abdalla, J. P. Berchem, J. Büchner, and L. M. Zelenyi, *J. Geophys. Res.* **98**, 5651 (1993).
- ¹¹D. C. Delcourt and J. A. Sauvaud, *J. Geophys. Res.* **99**, 97 (1994).
- ¹²I. Doxas, T. W. Speiser, P. B. Dusenbery, and W. Horton, *J. Geophys. Res.* **99**, 2375 (1994).
- ¹³J. Birn and M. Hesse, *J. Geophys. Res.* **99**, 109 (1994).
- ¹⁴G. Joyce, J. Chen, S. Slinker, D. L. Holland, and J. B. Harold, *J. Geophys. Res.* **100**, 19167 (1995).
- ¹⁵X. Li, D. N. Baker, M. Temerin, and G. D. Reeves, *Geophys. Res. Lett.* **25**, 3763 (1998).
- ¹⁶J. Birn, M. F. Thomsen, J. E. Borovsky, G. D. Reeves, D. J. McComas, R. D. Belian, and M. Hesse, *J. Geophys. Res.* **102**, 2325 (1997).
- ¹⁷J. Birn, M. F. Thomsen, J. E. Borovsky, G. D. Reeves, D. J. McComas, R. D. Belian, and M. Hesse, *J. Geophys. Res.* **103**, 9235 (1998).
- ¹⁸S. Zaharia, C. Z. Cheng, and J. R. Johnson, *J. Geophys. Res.* **105**, 18741 (2000).
- ¹⁹J. Büchner and L. Zelenyi, *J. Geophys. Res.* **92**, 13456 (1987).
- ²⁰J. Birn and M. Hesse, *J. Geophys. Res.* **101**, 15345 (1996).
- ²¹G. Erickson and R. Wolf, *Geophys. Res. Lett.* **7**, 897 (1980).
- ²²K. Schindler and J. Birn, *J. Geophys. Res.* **87**, 2263 (1982).
- ²³C. Chen and R. Wolf, *J. Geophys. Res.* **98**, 21409 (1993).
- ²⁴J. M. Quinn and D. J. Southwood, *J. Geophys. Res.* **87**, 10536 (1982).
- ²⁵B. H. Mauk, *J. Geophys. Res.* **91**, 13423 (1986).
- ²⁶T. G. Northrop, *The Adiabatic Motion of Charged Particles* (Wiley, New York, 1963).
- ²⁷A. A. Chan, *J. Geophys. Res.* **103**, 20501 (1998).
- ²⁸J. M. Hyman, *SIAM (Soc. Ind. Appl. Math.) J. Sci. Stat. Comput.* **4**, 645 (1983).
- ²⁹D. B. Curran and C. K. Goertz, *J. Geophys. Res.* **94**, 272 (1989).
- ³⁰L. R. Lyons, *J. Geophys. Res.* **89**, 5479 (1984).
- ³¹V. Vasyliunas, *J. Geophys. Res.* **73**, 2839 (1968).
- ³²S. P. Christon, D. J. Williams, and D. G. Mitchell, *J. Geophys. Res.* **96**, 1 (1991).